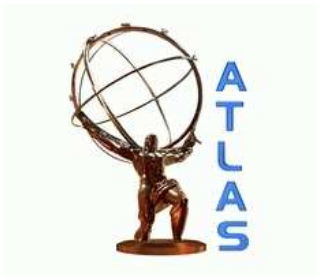

ATLAS NOTE

ATL-TILECAL-PUB-2008-004

March 14, 2008

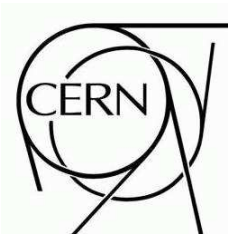

Time of Flight Analysis Using Cosmic Ray Muons in the ATLAS Tile Calorimeter

B. Meirose[1] and R.J. Teuscher[2, 3]

(1) UFRJ, Rio de Janeiro, Brazil,
(2) University of Toronto, Canada,
(3) Canadian Institute of Particle Physics (IPP)

Abstract

Using cosmic ray muon data recorded during the summer of 2007, we have studied the time-of-flight distributions between back-to-back modules of the ATLAS Tile Calorimeter. The results are in good agreement with the distributions expected from calorimeter geometry, and allow for cross-checks of timing corrections obtained in laser runs. Calorimeter timing is a useful tool to remove non-physics backgrounds, and we introduce new cuts at the cell level which improve the signal to noise ratio.

1 ATLAS experiment and Tile Calorimeter

The ATLAS (A Toroidal LHC ApparatuS) [1], [2] experiment is one of two general-purpose detectors under construction at the Large Hadron Collider (LHC) [3] at CERN [4]. Results from the LHC are expected to shed new light on the origin of electroweak symmetry breaking, and potentially open a wide spectrum of new physics discoveries. The main components of the ATLAS detector include the inner tracking detectors, the electromagnetic and hadronic calorimeters, and the muon spectrometers. This note focuses on a detailed timing analysis of cosmic ray muon signals in the ATLAS hadronic tile calorimeter (TileCal) [5]. Additional studies making use of the TileCal timing can be found in [6], [7], [8], [9], [10], [11], [12], [13], [14], [15], [16], [17], [18].

TileCal is a sampling calorimeter with iron absorber and scintillating plastic "tiles" as the active material, with a novel geometry of alternating layers perpendicular to the beam direction, and staggered in depth. This geometry provides a homogeneous sampling when the calorimeter is placed behind an electromagnetic compartment and a coil equivalent to about two interaction lengths of material.

The TileCal is a cylindrical structure with inner and outer radius of 2280 and 4230 mm respectively, located in the region $|\eta| < 1.7$, and is divided into three cylindrical sections; a barrel and two extended barrels. The barrel cylinder is 5640 mm in length along the beam axis, while each of the extended barrel cylinders is 2910 mm long. Each detector cylinder is built of 64 independent wedges along the azimuthal direction. Between the barrel and the extended barrels there is a gap of about 600 mm, which is needed for the Inner Detector and the electromagnetic calorimeter cables, electronics and services. The main function of the Tile Calorimeter is to contribute to the energy measurement of jets produced in pp interactions and, with the addition of the end-cap and forward calorimeters, to provide a good measurement of missing transverse momentum.

The light from each scintillating tile is transmitted on two sides by a wavelength-shifting fibre, and the fibres are bundled together to form readout cells of (0.1 x 0.1) in (ηxϕ) with three different sampling depths ((0.2 x 0.1) in the third sampling). Each cell is read out by two PMT's, one on either side, with a total of approximately 10000 PMT's in the entire TileCal. Figure 1 shows the Tile Calorimeter cells of one half barrel module and an extended barrel module, with the three independent longitudinal samplings labelled A, BC and D.

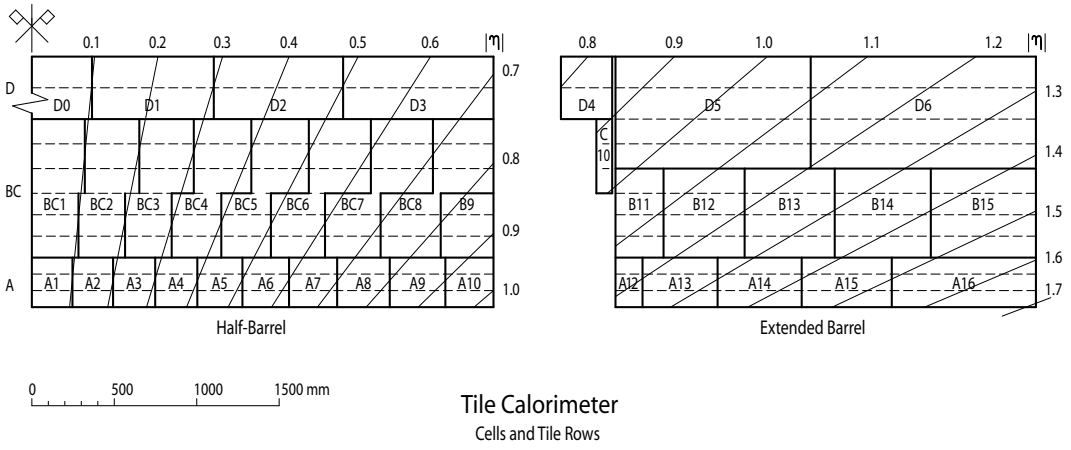

Figure 1: Cell geometry of one half of a TileCal barrel and extended barrel module. The fibers of each cell are routed to one PMT on each side. The PMT's are located in a rectangular girder region at the top (not shown).

The TileCal has excellent timing resolution, of order 1 ns per cell measuring energy deposits above

1 GeV. Timing resolution measurements for TileCal testbeam data can be found in references [19] and [20]. Calorimeter timing can be exploited to remove backgrounds, such as out-of-time cosmic rays, beam-gas events, beam-halo events, etc. Here we concentrate on the time-of-flight of cosmic ray muons in TileCal.

In Section 2 we give a brief summary of cosmic ray muon characteristics in the TileCal, define important quantities used along the analysis and estimate the predicted time of flight (TOF) from TileCal geometry. In Section 3 we analyze the time of flight distribution using three different approaches, comparing the measured values to the predicted ones and discuss the results. We also show in this section plots to motivate some of the cuts applied during the analysis. Our conclusions are summarized in Section 4.

2 Cosmic Rays in the Tile calorimeter

The analysis of cosmic ray muons [21] is a crucial step in the commissioning of the ATLAS calorimeters [22]. Typically muons deposit between 1 to 3 GeV in each projective tower of the TileCal, compared to an electronics noise of O(100) MeV per tower. A dedicated trigger has been constructed to allow for the triggering of cosmic ray muons in the TileCal [23], [24], [25]; this forms one of the main cosmic ray triggers for ATLAS commissioning.

One of the methods for separating cosmic ray signals from electronics noise in each cell is to study the time difference between the two PMT's per cell, here labelled "up" and "down". We expect in general the higher the signal energy, the smaller the cell time difference δt:

$$\delta t = T\,fit[up] - T\,fit[down] \tag{1}$$

where $T\,fit$ is the PMT time reconstructed from a least-squares fit [26] to the digitized pulse data. Note that the finite cell size limits the precision of the time difference to a few ns (see next section). The overall cell time is defined as t_{cell}, as:

$$t_{cell} = (T\,fit[up] + T\,fit[down])/2 \tag{2}$$

For the cell energy, we define:

$$E_{cell} = E\,fit[up] + E\,fit[down] \tag{3}$$

where $E\,fit[up(down)]$ is the energy reconstructed in each PMT calculated by a least-squares fit method [26].

In this paper we obtain the time of flight of muons in the TileCal between back-to-back (BTB) modules in the "A side" (i.e., BTB in ϕ) of the barrel (LBA19 and LBA51) but to improve statistics we perform part of the analysis with six pairs of modules (LBA14 to LBA19 with LBA46 to LBA51). When this is the case it is mentioned explicitly; for all other cases only one pair of modules is used. We calculate the time of flight as:

$$t_{flight} = t_{cell}(top) - t_{cell}(bot) \tag{4}$$

where $t_{cell}(top)$ and $t_{cell}(bot)$ are the top and bottom modules cell times respectively.

In this early stage of ATLAS commissioning, the intermodule timing calibrations were not yet available in a database. As consequence, we use the timing corrections obtained by [27] using laser runs. One of the purposes of this work was to crosscheck these laser time offsets.

To estimate the expected times of flights for muons travelling between the modules, we use the distances as in [28] and [5] considering that the muons travel close to the speed of light. As the cell distances are measured from each cell center, we use the cell sizes in the (η,ϕ) plane to estimate the maximum TOF error. Let x and y be the cell dimensions, such that the time of flight error is:

$$\sqrt{(x^2+y^2)}/c \tag{5}$$

where c is the speed of light. Although the cells have different sizes depending on layer, the largest differences are between A, BC and D cells (D cells have slightly different sizes but we take the largest D cell). By calculating the error in this way, we assume that the muon has an equal probability of traversing any part of the cell (this is a conservative estimate; strictly speaking only muons that go from cell center to cell center in the same side and from the same cell (A1 to A1 for example, see section 2.3) are truly vertical). We find for the times of flight expected from geometry for vertical A, BC and D cells (-16.2 ± 1.5) ns, (-19.8 ± 3.6) ns and (-24.2 ± 6.0) ns respectively.

When all cells are considered, the problem of obtaining a TOF for each cell group is less obvious because we are now considering all possible muon trajectories from the shortest (the vertical cells), to the longest, i.e., the first cell to the last cell (A1 to A8 for example). Nevertheless we make the approximation that that the highest contribution are from the vertical cells, and as we already considered the error within the limit of the largest cell size (for A, BC and D) this assumption is quite reasonable. This hypothesis will be checked with the measured TOF's values.

3 Data analysis

The data used in this present analysis were taken on July 27, 2007 and include 10626 events (run 16965), which was a calorimeter-only run triggered by the TileCal cosmic ray trigger. For reconstruction we use version 13.0.10 of the Athena software framework. We calculate the time of flight of muons using a series of cuts to maximize the signal-to-noise ratio, using information of the cell energy and PMT time difference per cell. Pedestal-like events, in which the signal reconstruction algorithm sets $Tfit[up(down)] = 0.00$, were removed from the sample. Well known hot cells from previous commissioning analysis were also removed. We will now apply a series of cuts on E_{cell} and $|\delta t|$ to demonstrate their successive improvement in the signal to noise ratio.

3.1 Cell time and PMT time difference versus cell energy

Figures 2 and 3 show E_{cell} as a function of $|\delta t|$ and t_{cell} for cells passing a first set of loose selection cuts, $E_{cell} > 100$MeV and $|\delta t| < 50$ ns. These cuts still retain a sufficient fraction of background so that it can be studied. All results in this section were obtained using six top TileCal modules (LBA14 to LBA19). Distributions for the bottom modules give similar results. The first plot is shown in Figure 2, which gives the cell energy versus the cell time difference $|\delta t|$. Note that most of the cell energy is concentrated in a small region below 6 ns. In order to balance signal to noise while retaining sufficient statistics, we apply a 6 ns time difference cut for the time of flight analysis (it is important to keep in mind that this is a box-plot, so the actual number of points can be a bit misleading; there are 1197 entries in the region above 6 ns, out of a total of 8099 entries). Note also that many of the high energy events with $E_{cell} > 10$GeV have a very low cell time difference $|\delta t|$. For reference, we also show in Figure 3 the cell energy versus the cell time t_{cell}.

3.2 Vertical Cells

In this section we compute the TOF for vertical A, BC, and D cells separately. Here we define vertical cells as the same cells in two opposite drawers, for example A1 in LBA19 and A1 in LBA51. This also allows a better comparison to the TOF expected from geometry, especially for the smaller A cells (here only vertical cells are being considered; when we include all possible cells in the next section we expect more deviations due the non-verticality of muons).

Figure 4 shows the TOF for vertical A cells between 6 pairs of modules of the TileCal barrel for a cell energy $E_{cell} > 100$ MeV. With this very loose cut on energy, it is not yet possible to obtain a meaningful

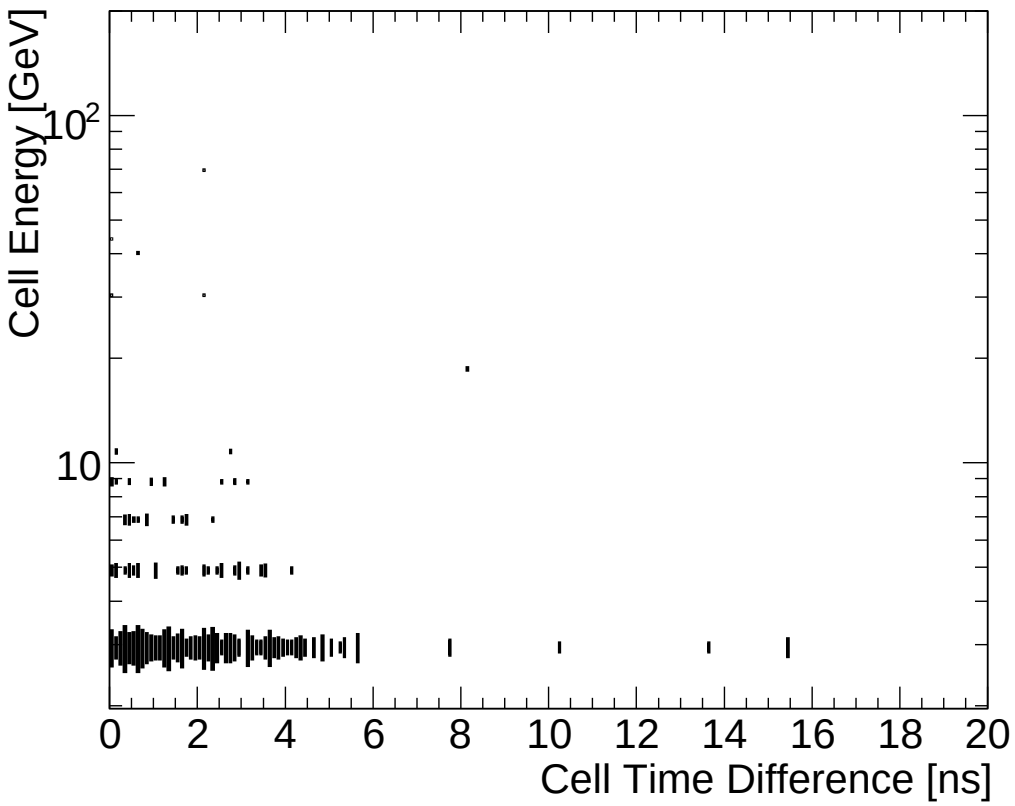

Figure 2: Cell energy E_{cell} versus the cell time difference $|\delta t|$ for six top TileCal barrel modules with $E_{cell} >$ 100 MeV and $|\delta t| < 50$ ns. Note that there are 1197 entries in the region of $|\delta t| > 6$ ns, out of a total of 8099 entries.

gaussian fit (see the Appendix B for plots for BC and D cells with the same cut) due the presence of background. To treat this problem we now study cuts on cell energy and cell time difference and show their effect. Then in the following section we further develop these cuts and the improvement becomes even more evident.

Figures 5, 6 and 7 show the time of flight for vertical cells (A, BC and D respectively) for a cell energy $E_{cell} > 200$ MeV and a cell time difference cut of $|\delta t| < 6$ ns. The statistics for the A cells are rather low(partly due to the small cell size, as smaller size implies shorter muon path length and therefore less energy deposited) but the result of the gaussian fit is encouraging: (-14.2 ± 0.5) ns, which is in agreement with the expected value from geometry (all fit errors were calculated as the gaussian width divided by the square-root of the number of entries). The statistics for BC cells are more than three times greater, and the fit gives (-18.1 ± 0.5) ns in good agreement with the expected value. For the D cells in Figure 7 it appears that a few cells have too low a TOF, which can be seen in the second peak around -11 ns. The statistics for the D cells are slightly lower than for the BC cells (i.e., the BC cells have the largest statistics because of the largest signal). The mean of the fitted gaussian distribution is around (-20.7 ± 0.7) ns. Investigating these events, we find they occur only between modules LBA17 and LBA49, which suggests the timing corrections for the D cells in those modules could further be improved. In Table 1 we summarize the expected and measured time of flight results for vertical cells with the above cuts.

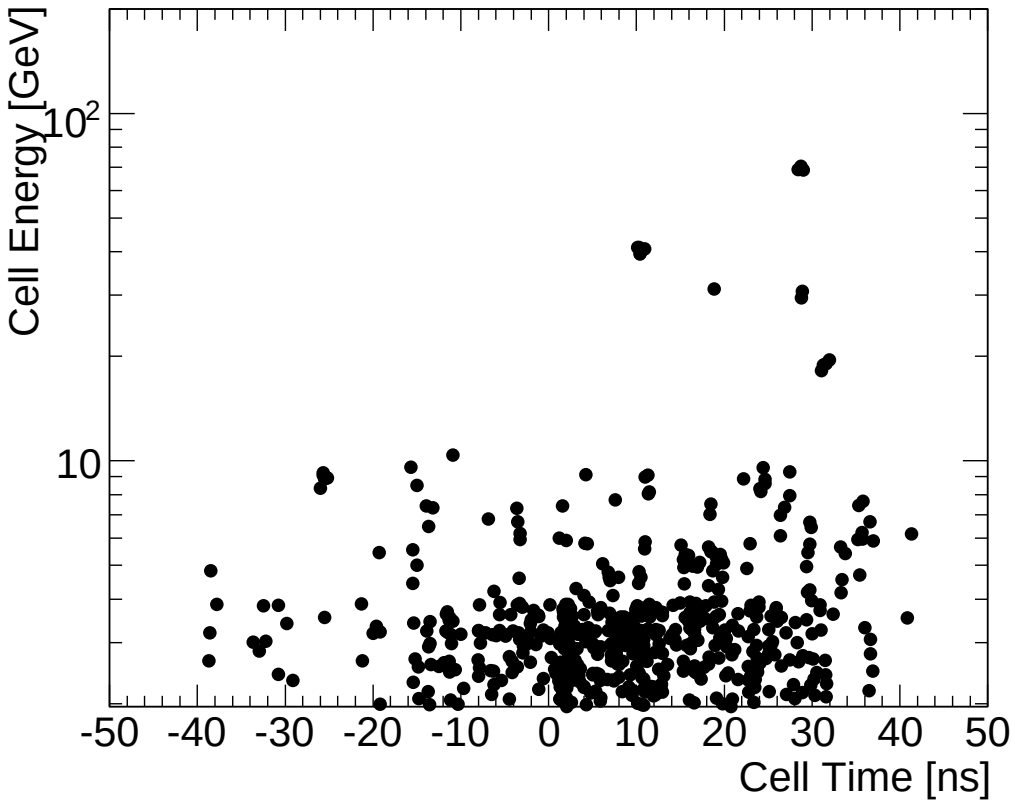

Figure 3: Cell energy E_{cell} versus the average cell time t_{cell} for six top barrel TileCal modules with $E_{cell} > 100$ MeV and $|\delta t| < 50$ ns.

3.3 Time of Flight for all cells

We now consider the TOF for all cells between one pair of BTB modules (LBA19 and LBA51), i.e., we calculate the TOF between an A (BC, D) cell on the top and and A (BC, D) cell on the bottom, which improves greatly the overall statistics. One complication that arises with this approach is that some events may contain multiple particles. To obtain the desired distributions we search for muons, i.e., any events that passed the cuts simultaneously, between the two modules. In the case of a two-muon event for example, we obtain the two correct muon TOF plus two "fake" muons (for example, suppose two real muons passed cells in LBA19 and LBA51 registering times ta and tb and t1 and t2 respectively. In this event we would get two entries (t1-ta) and (t2-tb), the correct ones, but because we do not know the actual muon path we register (t2-ta) and (t1-tb) as well, which are artificial entries); however, this effect is found to be small.

Figures 8 and 9 show the TOF distribution for all cells between two BTB modules for $E_{cell} > 100$ MeV for BC and D cells respectively. As expected the noise for both distributions is very high which can be seen by the high fluctuation on both sides of the peak of the distribution, especially in the region of positive times where one does not expect a signal. A plot for A cells give similar results.

Figures 10, 11 and 12 show the distribution for $E_{cell} > 100$ MeV, for A, BC and D cells respectively, but with a cell time difference cut of $|\delta t| < 6$ ns. It is clear that an improvement is made with this cut. For this time and energy cuts only the D cells gave the reasonable fit of (-19.2 ± 0.9) ns to be compared

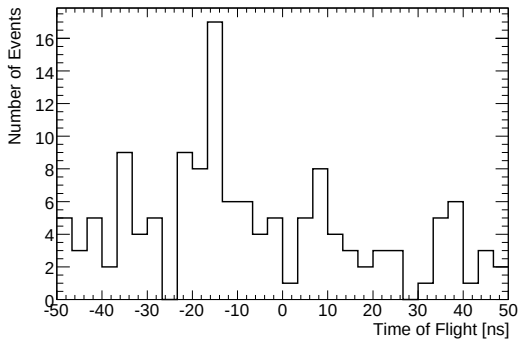

Figure 4: Time of flight distribution for vertical A cells with $E_{cell} > 100$ MeV.

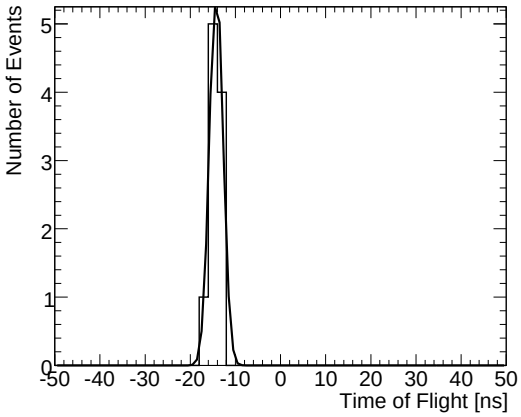

Figure 5: Time of flight distribution for vertical A cells with $E_{cell} > 200$ MeV and $|\delta t| < 6$ ns.

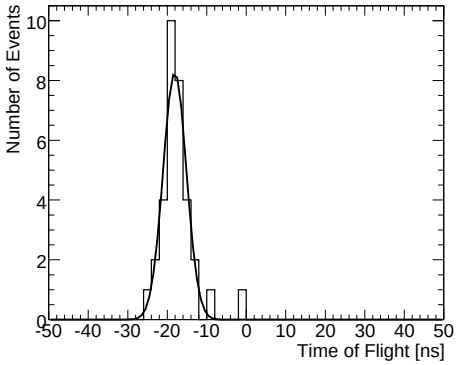

Figure 6: Time of flight distribution for vertical BC cells with $E_{cell} > 200$ MeV and $|\delta t| < 6$ ns.

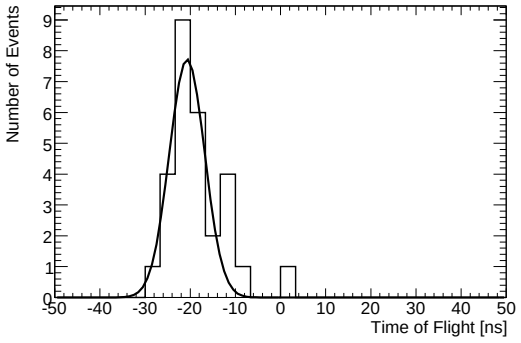

Figure 7: Time of flight distribution for vertical D cells with $E_{cell} > 200$ MeV and $|\delta t| < 6$ ns.

with (-19.8 ± 3.6) ns from the geometry.

Figure 13 shows the time of flight distribution for D cells with $E_{cell} > 200$ MeV. Much of the noise has been removed, and the few points remaining in the positive part of the plot, or with large negative times may be "fake muons" or exceptional noise fluctuations. The mean of the gaussian fit for Figure 13 is (-21.4 ± 0.6) ns. For BC cells the fitted value obtained is (-16.5 ± 0.4) ns. Due to residual background in the plot for A cells, in order to obtain a reasonable fit we must restrict the fit range to [-30,0] ns, for which we obtain a gaussian mean of (-14.7 ± 0.4) ns. Both plots for A and BC cells for this cut are shown in Appendix B. The results are summarized in Table 2. In Figure 14 the effect of a cell time difference cut of $|\delta t| < 6$ns for D cells for $E_{cell} > 200$ MeV is shown and the results for the three types of cells summarized in Table 3.

Finally we consider a cell energy cut of 400 MeV, which is shown in Figure 15 for BC cells and in Figure 16 for D cells. At this energy the noise is almost completely suppressed, but a few points with a low TOF are found, especially for the D cells. These outliers are completely removed when a cell time difference cut of $|\delta t| < 6$ns is applied, as shown in Figures 17 and 18. Results for the A cells can be found in Appendix B and suggest a less need of a $|\delta t|$ cut for this type of cell at this energy regime. Tables 4 and 5 show the expected and measured results for the plots in this energy range with

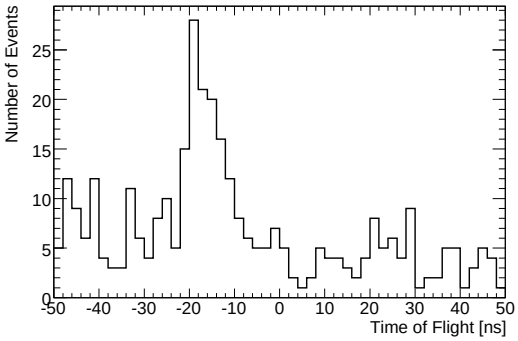

Figure 8: Time of flight distribution for all BC cells with $E_{cell} > 100$ MeV.

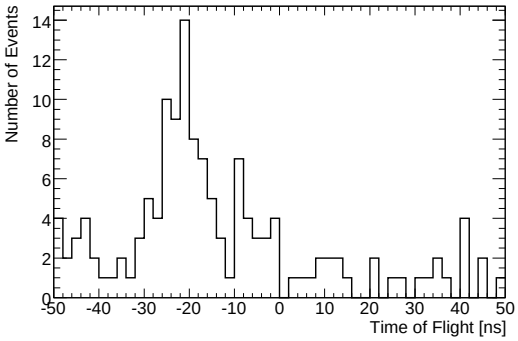

Figure 9: Time of flight distribution for all D cells with $E_{cell} > 100$ MeV.

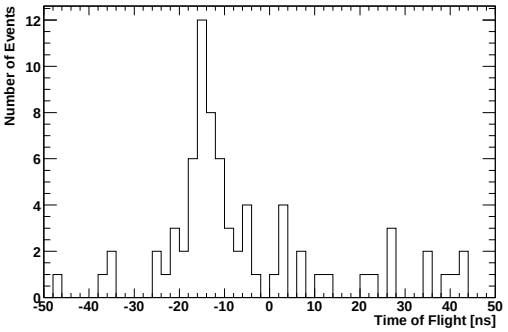

Figure 10: Time of flight distribution for all A cells with $E_{cell} > 100$ MeV and $|\delta t| < 6$ns.

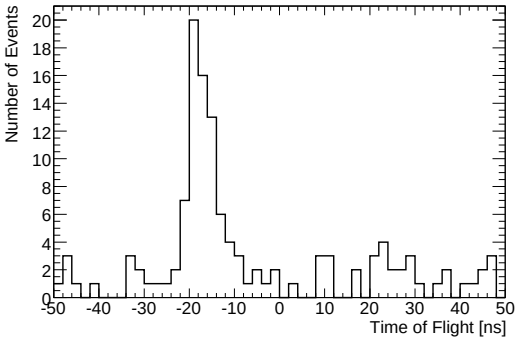

Figure 11: Time of flight distribution for all BC cells with $E_{cell} > 100$ MeV and $|\delta t| < 6$ns.

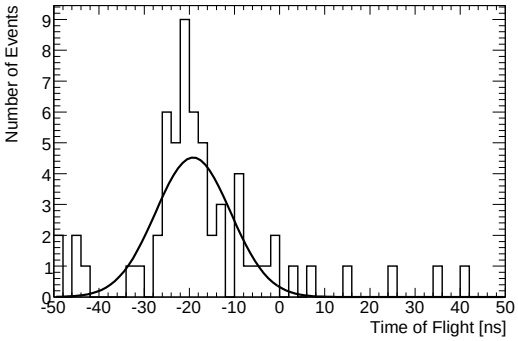

Figure 12: Time of flight distribution for all D cells with $E_{cell} > 100$ MeV and $|\delta t| < 6$ns.

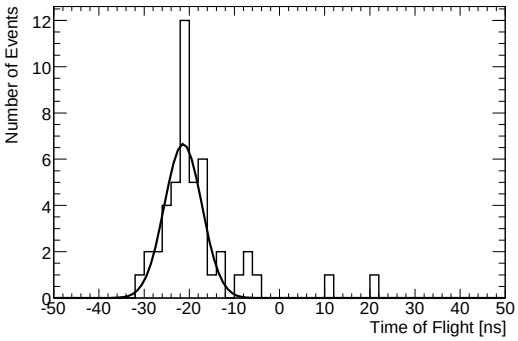

Figure 13: Time of flight distribution for all D cells with $E_{cell} > 200$ MeV.

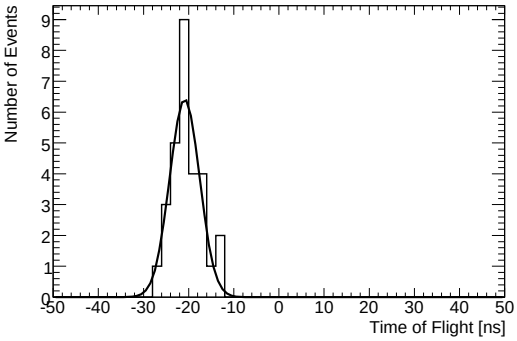

Figure 14: Time of flight distribution for all D cells with $E_{cell} > 200$ MeV and $|\delta t| < 6$ns.

Table 1: Predicted and experimental time of flight for vertical cells with $E_{cell} > 200$ MeV and $|\delta t| < 6$ ns.

Cell	Predicted TOF (ns)	Fitted TOF (ns)
A	-16.2±1.5	-14.2 ± 0.5
BC	-19.8±3.6	-18.1 ± 0.5
D	-24.2±6.0	-20.7 ± 0.7

Table 2: Predicted and measured time of flight for all cells as function of cell type with $E_{cell} > 200$ MeV.

Cell	Predicted TOF (ns)	Fitted TOF (ns)
A	-16.2±1.5	-14.7 ± 0.4
BC	-19.8±3.6	-16.5 ± 0.4
D	-24.2±6.0	-21.4 ± 0.6

and without a cell time difference cut respectively.

3.4 Average Time of Flight

Next we consider the average TOF for the muons for all cells. Now we expect a narrower width around the peak of the distributions, as the effect of mis-identified muons is reduced. The drawback of this approach is that one loses the more detailed cell information. To obtain the average TOF we simply sum all top and bottom cell times and calculate the average TOF, i.e.,:

$$A_{tflight} = \frac{\sum(t_{cell}(top) - t_{cell}(bot))}{N_{cells}} \tag{6}$$

where $A_{tflight}$ is the average TOF and N_{cells} is the number of selected cells. Note that with this approach we are always taking one entry per event, i.e., in the example we gave in the last section for the two muon event we would obtain $A_{tflight} = (t1 + t2 - ta - tb)/2$, i.e., we solved the problem of not knowing the actual muons tracks by taking the average.

In Figures 19 and 20 we record the average time of flight distribution for $E_{cell} > 100$ MeV for A and BC cells respectively. Due to the large noise contamination the peak is poorly resolved, especially for the A cells.

On the other hand the average time of flight distribution for $E_{cell} > 100$ MeV and $|\delta t| < 6$ns given in Figures 21 and 22 demonstrates the power of a cut on the cell time difference. For the A cells the improvement makes it already possible for one to obtain a gaussian fit of (-13.5 ± 0.4). This can be further improved with a tighter cut on cell energy. In Figure 23 we see the average TOF distribution

Table 3: Predicted and measured time of flight for all cells as function of cell type with $E_{cell} > 200$ MeV, with the additional requirement of $|\delta t| < 6$ns.

Cell	Predicted TOF (ns)	Fitted TOF (ns)
A	-16.2±1.5	-14.2 ± 0.5
BC	-19.8±3.6	-17.1 ± 0.4
D	-24.2±6.0	-20.9 ± 0.6

Table 4: Predicted and measured time of flight for all cells as function of cell type with $E_{cell} > 400$ MeV.

Cell	Predicted TOF (ns)	Fitted TOF (ns)
A	-16.2±1.5	-15.3 ± 0.8
BC	-19.8±3.6	-17.6 ± 0.3
D	-24.2±6.0	-21.3 ± 0.6

Table 5: Predicted and measured time of flight for all cells as function of cell type with $E_{cell} > 400$ MeV, with the additional requirement of $|\delta t| < 6$ns.

Cell	Predicted TOF (ns)	Fitted TOF (ns)
A	-16.2±1.5	-14.6 ± 0.9
BC	-19.8±3.6	-17.3 ± 0.3
D	-24.2±6.0	-21.1 ± 0.6

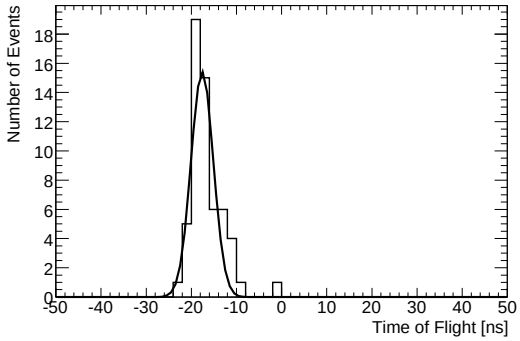

Figure 15: Time of flight distribution for all BC cells with $E_{cell} > 400$ MeV.

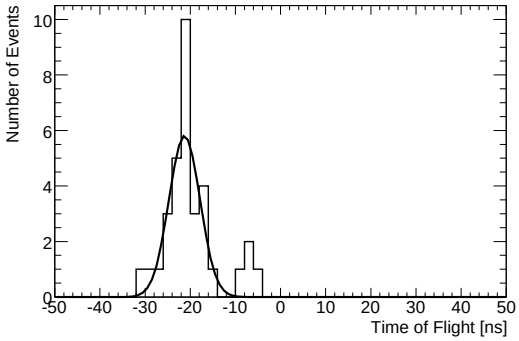

Figure 16: Time of flight distribution for all D cells with $E_{cell} > 400$ MeV.

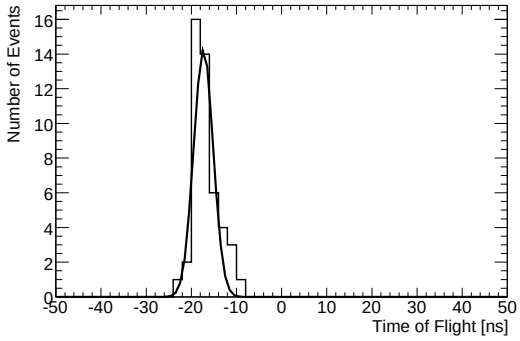

Figure 17: Time of flight distribution for all BC cells with $E_{cell} > 400$ MeV and $|\delta t| < 6$ns.

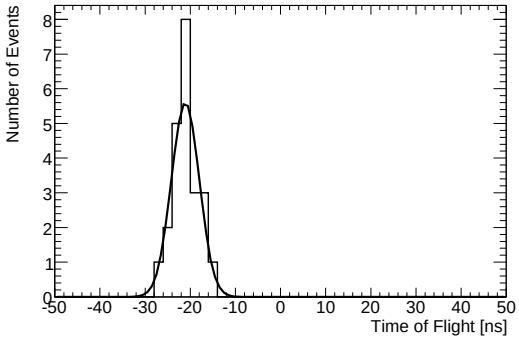

Figure 18: Time of flight distribution for all D cells with $E_{cell} > 400$ MeV and $|\delta t| < 6$ns.

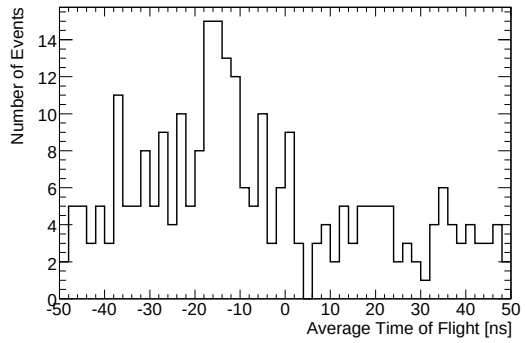

Figure 19: Average time of flight distribution for A cells with $E_{cell} > 100$ MeV.

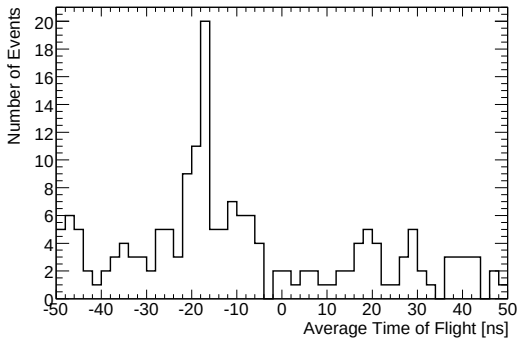

Figure 20: Average time of flight distribution for BC cells with $E_{cell} > 100$ MeV.

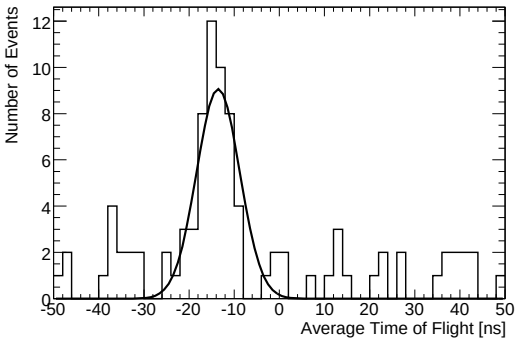

Figure 21: Average time of flight distribution for A cells with $E_{cell} > 100$ MeV and $|\delta t| <$ 6ns.

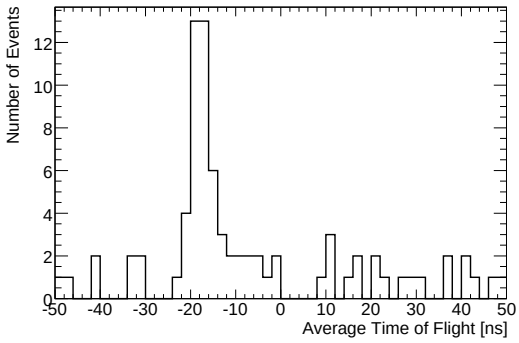

Figure 22: Average time of flight distribution for BC cells with $E_{cell} > 100$ MeV and $|\delta t| <$ 6ns.

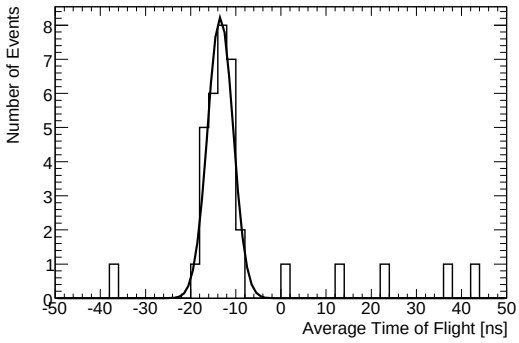

Figure 23: Average time of flight distribution for A cells with $E_{cell} > 200$ MeV and $|\delta t| <$ 6ns.

Table 6: Predicted and experimental average time with $E_{cell} > 200$ MeV and $|\delta t| < 6$ ns as a function of cell type.

Cell	Predicted TOF (ns)	Fitted TOF (ns)
A	-16.2±1.5	-13.4 ± 0.5
BC	-19.8±3.6	-17.7 ± 0.3
D	-24.2±6.0	-21.4 ± 0.7

for $E_{cell} > 200$ MeV and $|\delta t| < 6$ns. A few noise entries remain in the positive part of the histogram. The gaussian fit for Figure 23 is around (-13.5 ± 0.4)ns. The plots for BC and D cells can be found in Appendix B. In Table 6 we summarize the expected and measured average time of flight results as a function of cell type for $E_{cell} > 200$ MeV and $|\delta t| < 6$ns.

To refine the average TOF distributions we apply the cut $E_{cell} > 400$ MeV, shown in Figure 24 for D cells. Because of some few remaining points with too-low a TOF the gaussian fit does not appear very reliable. The problem is solved with a $|\delta t|$ cut of 6 ns shown in Figure 25. In Appendix B it is possible to find similar results for A and BC cells and in Table 7 we summarize the fits for the averages TOF's with $E_{cell} > 400$ MeV and $|\delta t| < 6$ ns. In order to improve the statistics, the result for six pairs of top-bottom modules (six on the bottom and six on the top, LBA14 to LBA19 with LBA46 to LBA51) are shown in Figures 26, 27 and 28, for A, BC and D cells respectively. For all plots it is possible to observe an increase of a small extra peak around -10ns, showing that it is an effect present in more than one pair of modules and for the three types of cells. In Table 8 the TOF fitted results for $E_{cell} > 400$ MeV using 6 pairs of modules are summarized.

Table 7: Predicted and experimental average time with $E_{cell} > 400$ MeV and $|\delta t| < 6$ ns as a function of cell type.

Cell	Predicted TOF (ns)	Fitted TOF (ns)
A	-16.2±1.5	-13.9 ± 0.6
BC	-19.8±3.6	-17.7 ± 0.3
D	-24.2±6.0	-21.7 ± 0.8

Table 8: Predicted and measured time of flight for all cells as function of cell type, for six pairs of barrel modules, with $E_{cell} > 400$ MeV.

Cell	Predicted TOF (ns)	Fitted TOF (ns)
A	-16.2±1.5	-14.4 ± 0.2
BC	-19.8±3.6	-18.8 ± 0.2
D	-24.2±6.0	-20.4 ± 0.5

3.5 Cell time, cell energy and $|\delta t|$ vs TOF

To complete the discussion, we show three distributions relating to the cuts used in the above analysis. Here we apply the same cuts as in section 3.1 using the same six top modules (LBA14 to LBA19).

The first distribution is the cell energy for the modules, shown in Figure 29. The cell energy is concentrated in a small region that peaks below 1 GeV, followed by a second smaller region up to 19

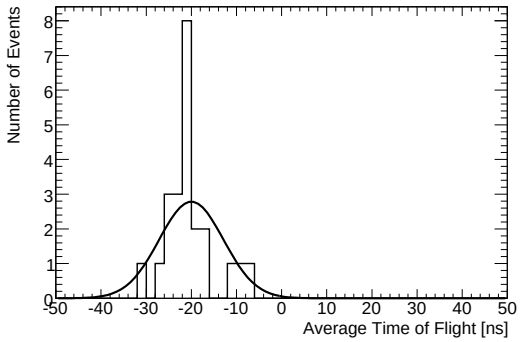

Figure 24: Average time of flight distribution for D cells with $E_{cell} > 400$ MeV.

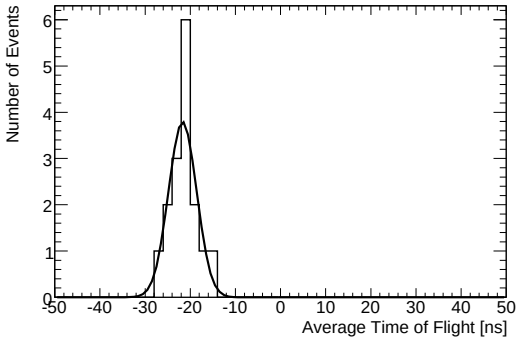

Figure 25: Average time of flight distribution for D cells with $E_{cell} > 400$ MeV and $|\delta t| <$ 6ns.

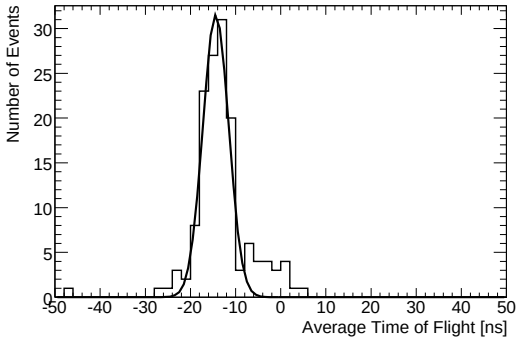

Figure 26: Average time of flight distribution for A cells, for six pairs of barrel modules, with $E_{cell} > 400$ MeV.

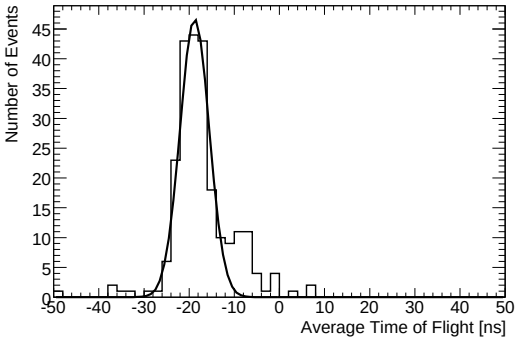

Figure 27: Average time of flight distribution for BC cells, for six pairs of barrel modules, with $E_{cell} > 400$ MeV.

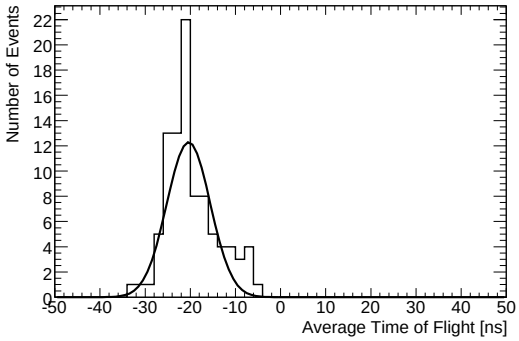

Figure 28: Average time of flight distribution for D cells, for six pairs of barrel modules, with $E_{cell} > 400$ MeV.

GeV. Most of the events concentrated in the low-energy region arise from electronics noise. Some hard bremsstrahlung events with $E_{cell} > 30$GeV (and a few events with $E_{cell} > 50$GeV) are also observed, but are not shown in the plot for clarity. For comparison, Figure 30 gives the same cell energy distribution but with a tighter cut of $|\delta t| < 6$ ns.

Next we show the cell time distribution with a cut of $|\delta t| < 50$ ns in Figure 31, and with $|\delta t| < 6$ ns in Figure 32. The mean of the first distribution is 3.4 ns due to the fact that the low energy cut has slightly biased the distribution.

The plot in Figure 33 shows the cell time difference $|\delta t|$ versus the time of flight between the modules. Note the densely-populated region around the value of -20ns; the smaller the value of $|\delta t|$ in this region more clustered the points. This demonstrates again the use of a cut on cell time difference in selecting signal events.

4 Conclusions

We have calculated the time of flight of cosmic ray muons between back-to-back modules of the Tile Calorimeter barrel using three different techniques, developing cuts on the cell time difference and cell energy. These results are in good agreement with the expected time of flight from geometry.

We first calculated the time of flight for vertical muons, separating the three types of TileCal barrel cells A, BC and D. The results of the gaussian mean for the three types of cells are in good agreement with the expected value, although the statistics for the A cells were low. We also find that a few D cells give unexpected times of flight between modules LBA17 and LBA49.

Then we obtained the time of flight distributions for all A, BC and D cells. The effect of misidentified muons due to electronics noise is found to be small. After a cut of 400 MeV in the cell energy and 6 ns in the cell time difference the time of flight distributions contain very little noise and the mean of the gaussian for the distribution is in very good agreement with the expected value.

We have studied selection cuts to improve the signal-to-noise ratio, and find that cuts on cell energy of 400 MeV and time difference of 6 ns are sufficient for this study. The results have been expanded to six pairs of top-bottom modules, improving the overall statistics. All times of flight calculated in this paper were made using timing corrections obtained with laser runs studies, and we conclude that in the majority of cases they were in agreement with the expected results.

5 Acknowledgements

B. Meirose would like to acknowledge the support of CNPq in this project. We would also like to acknowledge the many efforts of the commissioning communities in the TileCal, LAr, and offline software teams.

References

[1] ATLAS Collaboration, The ATLAS Experiment at the CERN Large Hadron Collider, (submitted to JINST, 2008).

[2] ATLAS Collaboration, ATLAS Technical Proposal, (CERN/LHCC/94-43, 1994).

[3] LHC Homepage http://lhc.web.cern.ch/lhc/.

[4] CERN Homepage http://www.cern.ch.

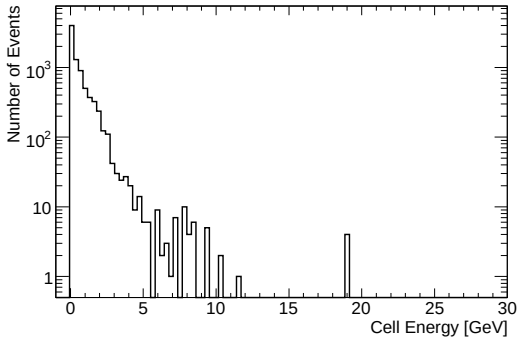

Figure 29: Cell energy distribution for six top barrel modules with $E_{cell} > 100$MeV and $|\delta t| < 50$ns.

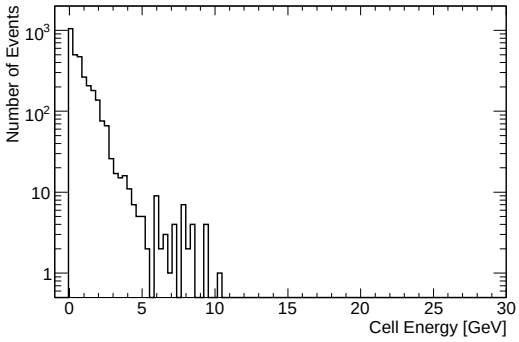

Figure 30: Cell energy distribution for six top barrel TileCal modules with $E_{cell} > 100$MeV and $|\delta t| < 6$ns.

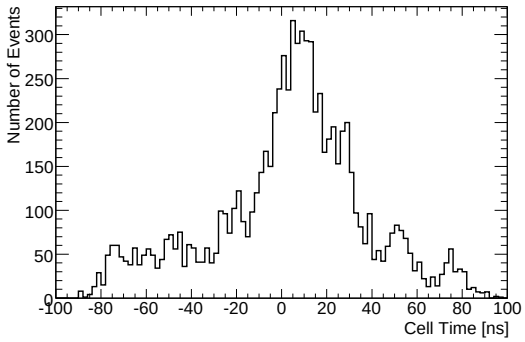

Figure 31: Average cell time distribution for six top barrel TileCal modules with $E_{cell} > 100$MeV and $|\delta t| < 50$ns.

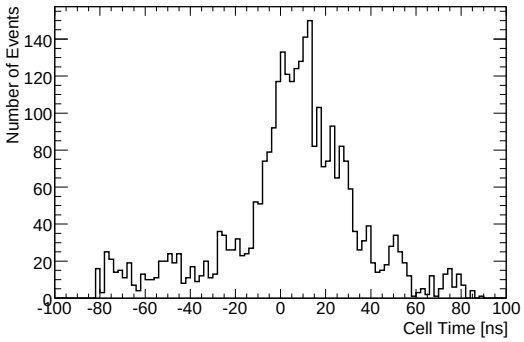

Figure 32: Average cell time distribution for six top barrel TileCal modules with $E_{cell} > 100$MeV and $|\delta t| < 6$ns.

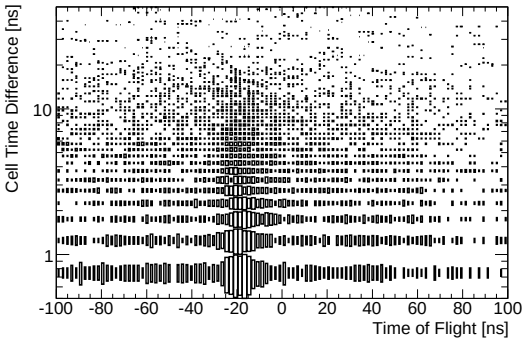

Figure 33: Cell time difference versus time of flight for six top barrel modules with $E_{cell} > 100$MeV and $|\delta t| < 50$ns.

[5] ATLAS Collaboration, ATLAS Tile Calorimeter Technical Design Report, (CERN/LHCC/96-42, CERN, 1996).

[6] R.J. Teuscher *et al*, Fake $\not\!\!E_T$ from ATLAS calorimeter cosmic ray data, CERN, ATL-COM-CAL-2008-002 (2008).

[7] C. Bohm, S. Hellman, K. Jon-And, J. Lesser, M. Ramstedt, ATLAS TileCal Timing, CERN, ATL-TILECAL-2004-008 (2004).

[8] O. Solovvyanov, Tile Calorimeter timing, TileCal Electronics, July 17, 2007, web page: http://indico.cern.ch/materialDisplay.py?contribId=8&materialId=slides&confId=18758.

[9] M. Cooke *et al*, *In situ* commissioning of the ATLAS electromagnetic calorimeter with cosmic muons, CERN, ATL-LARG-PUB-2007-013 (2007).

[10] C. Clement, TileCal Timing, TileCal Calibration Workshop, November 12, 2008, web page: http://indico.cern.ch/materialDisplay.py?contribId=8&sessionId=2&materialId=slides&confId=23070.

[11] F. Vives, Timing with cosmic runs from M4, TileCal Performance, October 1, 2007, web page: http://indico.cern.ch/materialDisplay.py?contribId=0&materialId=slides&confId=21982.

[12] B. Nordqvist, C. Clement, Timing equalization with Laser and LED data in TileCal, web page: http://indico.cern.ch/conferenceDisplay.py?confId=18753.

[13] G. Schlager, M. Flechl, M. Aleksa, Timing with Cosmics in TileCal, TileCal Commissioning, November 24, 2005, web page: http://indico.cern.ch/materialDisplay.py?contribId=s1t2&materialId=0&confId=a057757.

[14] M. Aleksa, LAr Studies on the LAr and Tile Combined Cosmic Runs, TileCal Performance, July 17, 2007, web page: http://indico.cern.ch/materialDisplay.py?contribId=18&sessionId=0&materialId=slides&confId=18753.

[15] J. Maneira, Timing Corrections with Cosmics, TileCal Performance, January 29, 2007, web page: http://indico.cern.ch/materialDisplay.py?contribId=9&materialId=slides&confId=10918.

[16] J. Maneira, R. Teuscher, Lessons from Cosmics, TileCal Commissioning, July 17, 2007, web page: http://indico.cern.ch/materialDisplay.py?contribId=17&sessionId=0&materialId=slides&confId=18753.

[17] S. Posen, Timing and Compliation Statistics, TileCal Performance Meeting, August 20, 2007, web page: http://indico.cern.ch/materialDisplay.py?contribId=5&materialId=slides& confId=20085.

[18] J. Maneira, R. Teuscher, Calorimeter Calibration Using Cosmic Rays, TileCal Calibration Workshop, November 13, 2007, web page: http://indico.cern.ch/conferenceDisplay.py?confId=23070.

[19] T. Del Prete, I. Vivarelli, The Timing of the Tile Calorimeter using laser events, CERN, "ATL-TILECAL-2003-009" (2003).

[20] R. Leitner, V. V. Shmakova, P. Tas, Time resolution of the ATLAS Tile Calorimeter and its performance for a measurement of heavy stable particles, CERN, "ATL-TILECAL-PUB" (2007).

[21] Claus Grupen, Astroparticle Physics, (Springer, Germany, 2005).

[22] R. Teuscher, Commissioning with Physics data at ATLAS, ICHEP2005, Proceedings, ATL-COM-SLIDE-2006-001.

[23] K. Anderson, J. Pilcher, H. Sanders, F. Tang, R. Teuscher, Stand-alone Cosmic Ray Trigger Electronics for the ATLAS Tile Calorimeter, 2004.

[24] R. Teuscher, News from TileCal cosmic ray trigger, web page: http://indico.cern.ch/conferenceDisplay.py?confId=a0626.

[25] An additional 4 coincidence boards were later constructed by the Grenoble ATLAS group and used for combined cosmic ray commissioning.

[26] R. Teuscher, T. Davidek, Reference on Electronics CIS Calibration and Energy Reconstruction, TileCal Commissioning, July 14, 2004, web page: http://indico.cern.ch/conferenceDisplay.py?confId=a043191.

[27] C. Clement, Laser Timing Dskews, web page: http://atlas-sw.cern.ch/cgi-bin/viewcvs-atlas.cgi/groups/stockholm/TileCal/LaserTiming/Dskews/.

[28] L. M. de Andrade Filho, Tile Cosmic View Program, web page: http://atlas-sw.cern.ch/cgi-bin/cvsweb.cgi/offline/TileCalorimeter/TileMonitoring/team5/TileCosmicView/?cvsroot=atlasślax .

Appendices

A Lengths used for Time of Flight calculation

In Table 9 we show the distances used for the time of flight calculation. All distances are from center-to-center. Note that the distances are between the same cells, i.e., for A cells from A1 to A1, A2 to A2, etc. The same is true for B, C and D. Note also that the final BC TOF that was used in the note was taken as the average TOF between B and C.

Table 9: Vertical cell distances (center to center) for TileCal barrel, side A.

Cell	Distance (mm)	Predicted TOF (ns)
A	4863.24	-16.21
B	5543.36	-18.48
C	6353.82	-21.18
D	7277.06	-24.26

B Times of flight with cell energy and time difference cuts

In Figures 34 and 35 we show the TOF for vertical BC and D cells respectively. As for the A cells, for the BC cells it was not possible to obtain a meaningful gaussian fit, but for the D cells despite the presence of noise the fitted value is (-20.5 ± 0.62)ns which is already in good agreement with the prediction of (-24.2 ± 6.0)ns from geometry.

In figures 36 and 37 we show the TOF for BC and A cells respectively, with a $E_{cell} > 100$ MeV cut. Figures 38 and 39 show the TOF for BC cells with $E_{cell} > 400$ MeV, without and with a $|\delta t| < 6$ns cut respectively.

Figures 40 and 41 show the average TOF for D cells with $E_{cell} > 400$ MeV, without and with a $|\delta t| < 6$ns cut respectively. In figures 42 and 43 the average TOF is shown for BC and D cells respectively, with $E_{cell} > 200$ MeV and $|\delta t| < 6$ns cut. Figures 44, 45, 46 and 47 show the average TOF for A and BC cells with $E_{cell} > 400$ MeV, the first two without a cell time difference cut of 6ns and the two last with the cut applied.

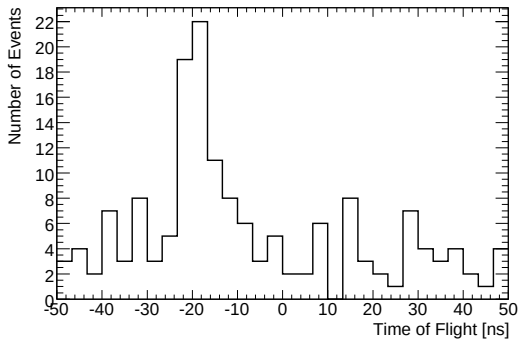

Figure 34: Time of flight distribution for vertical BC cells with $E_{cell} > 100$ MeV.

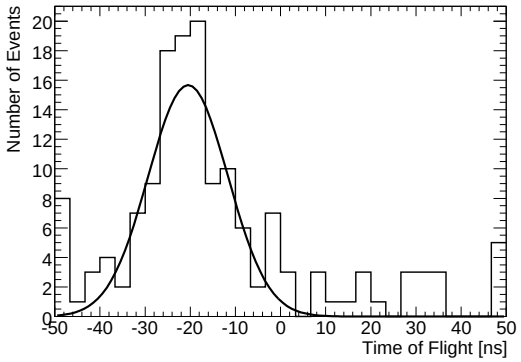

Figure 35: Time of flight distribution for vertical D cells with $E_{cell} > 100$ MeV.

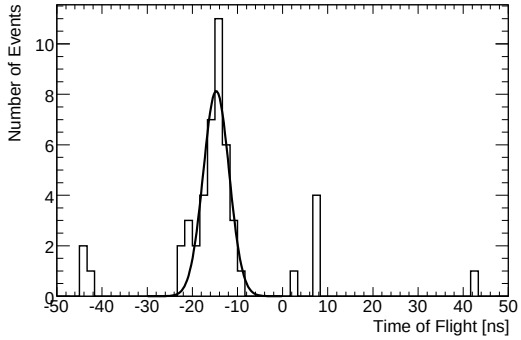

Figure 36: Time of flight distribution for all A cells with $E_{cell} > 200$ MeV.

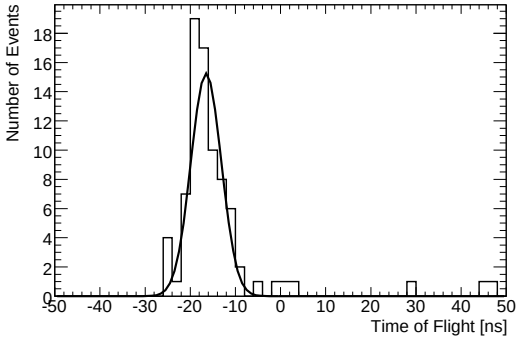

Figure 37: Time of flight distribution for all BC cells with $E_{cell} > 200$ MeV.

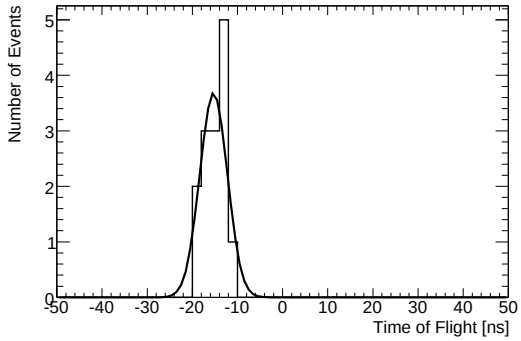

Figure 38: Time of flight distribution for all A cells with $E_{cell} > 400$ MeV.

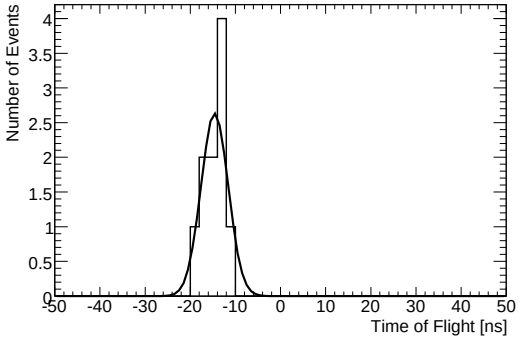

Figure 39: Time of flight distribution for all A cells with $E_{cell} > 400$ MeV and $|\delta t| < 6$ns.

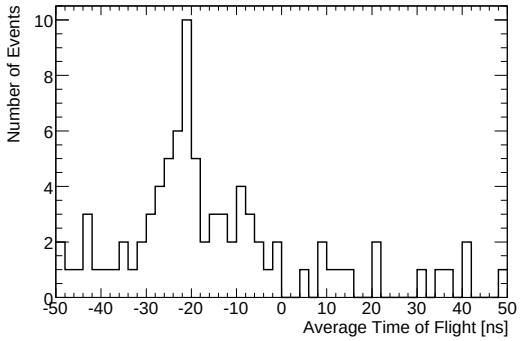

Figure 40: Average time of flight distribution for D cells with $E_{cell} > 100$ MeV.

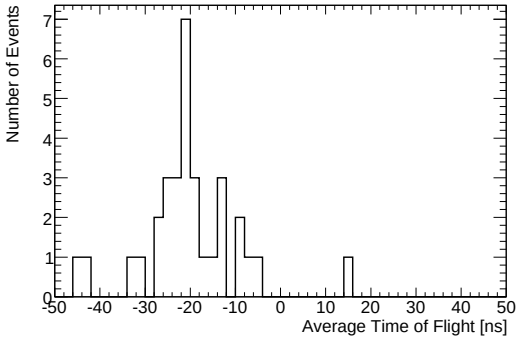

Figure 41: Average time of flight distribution for D cells with $E_{cell} > 100$ MeV and $|\delta t| <$ 6ns.

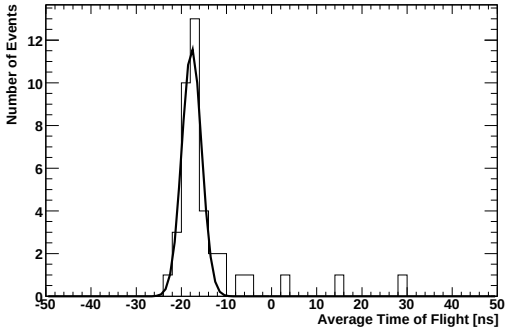

Figure 42: Average time of flight distribution for BC cells with $E_{cell} > 200$ MeV and $|\delta t| <$ 6ns.

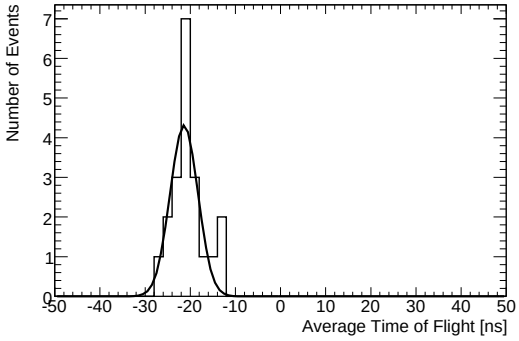

Figure 43: Average time of flight distribution for D cells with $E_{cell} > 200$ MeV and $|\delta t| <$ 6ns.

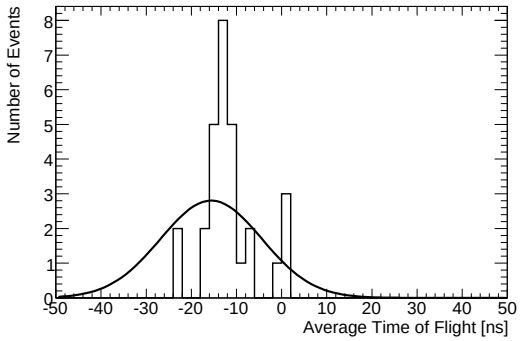

Figure 44: Average time of flight distribution for A cells with $E_{cell} > 400$ MeV.

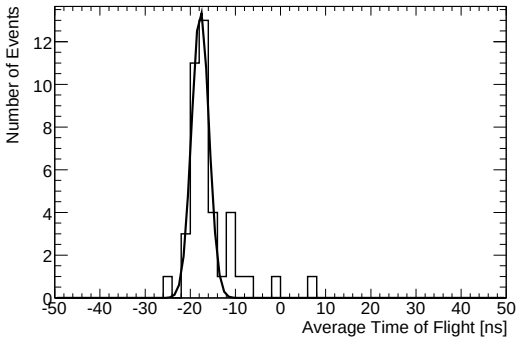

Figure 45: Average time of flight distribution for BC cells with $E_{cell} > 400$ MeV.

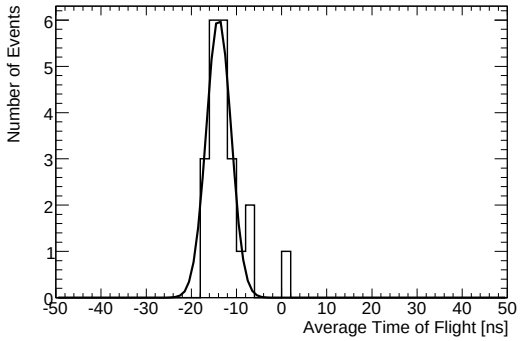

Figure 46: Average time of flight distribution for A cells with $E_{cell} > 400$ MeV and $|\delta t| <$ 6ns.

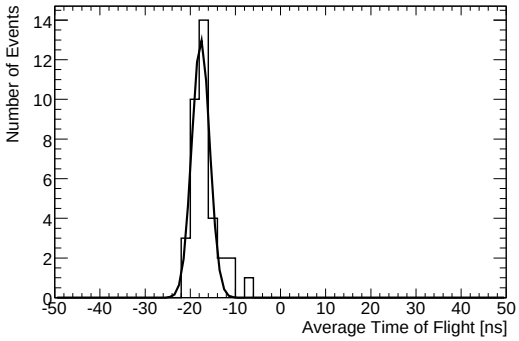

Figure 47: Average time of flight distribution for BC cells with $E_{cell} > 400$ MeV and $|\delta t| <$ 6ns.